

## New measurement of the $^{11}\text{B}(p,\alpha_0)^8\text{Be}$ bare-nucleus $S(E)$ factor via the Trojan horse method

This article has been downloaded from IOPscience. Please scroll down to see the full text article.

2012 J. Phys. G: Nucl. Part. Phys. 39 015106

(<http://iopscience.iop.org/0954-3899/39/1/015106>)

View [the table of contents for this issue](#), or go to the [journal homepage](#) for more

Download details:

IP Address: 143.107.255.190

The article was downloaded on 02/07/2012 at 20:39

Please note that [terms and conditions apply](#).

# New measurement of the $^{11}\text{B}(p,\alpha_0)^8\text{Be}$ bare-nucleus $S(E)$ factor via the Trojan horse method

L Lamia<sup>1,2</sup>, C Spitaleri<sup>1,2</sup>, V Burjan<sup>3</sup>, N Carlin<sup>4</sup>, S Cherubini<sup>1,2</sup>,  
V Crucillà<sup>1,2</sup>, M Gameiro Munhoz<sup>4</sup>, M Gimenez Del Santo<sup>4</sup>,  
M Gulino<sup>1,2</sup>, Z Hons<sup>3</sup>, G G Kiss<sup>5</sup>, V Kroha<sup>3</sup>, S Kubono<sup>6</sup>,  
M La Cognata<sup>1,2</sup>, C Li<sup>7,8</sup>, J Mrazek<sup>3</sup>, A Mukhamedzhanov<sup>9</sup>,  
R G Pizzone<sup>1,2</sup>, S M R Puglia<sup>1,2</sup>, Q Wen<sup>7</sup>, G G Rapisarda<sup>1,2</sup>, C Rolfs<sup>10</sup>,  
S Romano<sup>1,2</sup>, M L Sergi<sup>1,2</sup>, E Somorjai<sup>5</sup>, F A Souza<sup>4,11</sup>,  
A Szanto de Toledo<sup>4</sup>, G Tabacaru<sup>8</sup>, A Tumino<sup>1,2,12</sup>, Y Wakabayashi<sup>6</sup>,  
H Yamaguchi<sup>6</sup> and S-H Zhou<sup>7</sup>

<sup>1</sup> Laboratori Nazionali del Sud, INFN, Catania, Italy

<sup>2</sup> Dipartimento di Fisica e Astronomia, Università degli Studi di Catania, Italy

<sup>3</sup> Institute for Nuclear Physics, Prague-Rez, Czech Republic

<sup>4</sup> Departamento de Física Nuclear, Universidade de São Paulo, São Paulo, Brasil

<sup>5</sup> Atomki, Debrecen, Hungary

<sup>6</sup> CNS-University of Tokyo, Japan

<sup>7</sup> China Institute of Energy, Beijing, People's Republic of China

<sup>8</sup> Beijing Radiation Center, 100875 Beijing, People's Republic of China

<sup>9</sup> Cyclotron Institute, Texas A&M University, College Station, TX 77843, USA

<sup>10</sup> Ruhr-Universität, Bochum, Germany

<sup>11</sup> Instituto de Pesquisas Energéticas e Nucleares, IPEN-CNEN/SP, São Paulo, Brasil

E-mail: [llamia@lns.infn.it](mailto:llamia@lns.infn.it)

Received 24 June 2011

Published 1 December 2011

Online at [stacks.iop.org/JPhysG/39/015106](http://stacks.iop.org/JPhysG/39/015106)

## Abstract

A new measurement of the  $^{11}\text{B}(p,\alpha_0)^8\text{Be}$  has been performed applying the Trojan horse method (THM) to the  $^2\text{H}(^{11}\text{B},\alpha_0^8\text{Be})\text{n}$  quasi-free reaction induced at a laboratory energy of 27 MeV. The astrophysical  $S(E)$  factor has been extracted from  $\sim 600$  keV down to zero energy by means of an improved data analysis technique and it has been compared with direct data available in the literature. The range investigated here overlaps with the energy region of the light element LiBeB stellar burning and with that of future aneutronic fusion power plants using the  $^{11}\text{B}+p$  fuel cycle. The new investigation described here confirms the preliminary results obtained in the recent TH works. The origin of the discrepancy between the direct estimate of the  $^{11}\text{B}(p,\alpha_0)^8\text{Be}$   $S(E)$ -factor at zero energy and that from a previous THM investigation is quantitatively corroborated. The results obtained here support, within the

<sup>12</sup> Present address: Università degli Studi di Enna 'Kore', Enna, Italy.

experimental uncertainties, the low-energy  $S(E)$ -factor extrapolation and the value of the electron screening potential deduced from direct measurements.

(Some figures may appear in colour only in the online journal)

## 1. Introduction

The possibility of extracting simultaneously the residual abundances of the three light elements lithium, beryllium and boron (here and after LiBeB) in young stellar atmospheres has been addressed in the last 30 years as a possible probe for a deeper understanding of plasma mixing phenomena inside stars. Different authors ([1] and references therein) suggest in fact that the study of LiBeB abundances in young main sequence F and G stars can give useful information on different stellar mixing processes not fully understood yet. For these type of stars, having a temperature in the range  $5000 \text{ K} < T_{\text{eff}} < 7500 \text{ K}$ , standard stellar models do not take into account the possibility of ‘communication’ between the convective zone and the nuclear destruction zone where the burning occurs mainly via  $(p,\alpha)$  reactions at  $2 \times 10^6 \text{ K}$  for lithium,  $3.5 \times 10^6 \text{ K}$  for beryllium and  $5 \times 10^6 \text{ K}$  for boron. This means that the residual amount of LiBeB would reflect the abundances of the original interstellar gas and then no variations would be expected with respect to the reference, e.g. meteoritic, abundances [2]. The ‘light element LiBeB problem’, appeared with the earlier studies on Li abundances in Hyades ( $\sim 600 \text{ My}$ ) and in Pleiades ( $\sim 70 \text{ My}$ ) open clusters ([1] and references therein), has been powered over the years by different observational evidence as well as the less-pronounced Be-dip connected with the Li-dip in coeval open clusters, the constancy of B abundances as the stellar temperature varies, and the Li-Be and the Be-B correlation [3–5]. In spite of standard stellar models that ignore magnetic fields, mass loss or rotation, the observational status suggests that for F main-sequence young stars, there is a depletion of lithium and beryllium as detected in Hyades, Praesepe ( $\sim 600 \text{ My}$ ) and on other young clusters, while there is no evidence of this depletion in F pre-main sequence stars as the observations on Pleiades cluster ( $\sim 70 \text{ My}$ ) reveal [3]. The discrepancies between the observations and the stellar models could be overcome if mixing phenomena induced, for example, by stellar rotation are taken into account [1, 2].

However, to understand if the current discrepancies are only due to a not well-established theoretical description of the stellar mixing phenomena,  $(p,\alpha)$  nuclear reaction cross sections must be carefully evaluated right in the energy region corresponding to the typical stellar interiors.

The energy region, known as the Gamow window, depends on the astrophysical environment where the reaction takes place. Its center  $E_0$  and width  $\Delta E_0$  are given by [6]

$$E_0 = 1.22(Z_x^2 Z_X^2 \mu T_6^2)^{\frac{1}{3}} \text{ keV}$$

$$\Delta E_0 = 0.749(Z_x^2 Z_X^2 \mu T_6^5)^{\frac{1}{6}} \text{ keV},$$

where  $x$  and  $X$  are the two interacting particles in the entrance channel,  $\mu$  their reduced mass and  $T_6$  the temperature of the stellar plasma, in millions of kelvin. If one considers, for example, the  $^{11}\text{B}(p,\alpha)^8\text{Be}$  nuclear burning at a temperature of  $T_6 \sim 5$ , one obtains  $E_0 \sim 10 \text{ keV}$  and  $\Delta E_0 \sim 5 \text{ keV}$ .

The direct measurement of a charged-particle reaction at astrophysical energies is often hindered by the Coulomb barrier between the interacting nuclei, usually of the order of

$\sim$ MeV, drastically reducing the reaction cross section to the scale of picobarn or to lower values. Moreover, in spite of several improvements in the experimental techniques to explore the Gamow window, the presence of the electron screening [6–8], due to the electronic cloud surrounding the interacting ions, prevents one measuring the bare nucleus cross section  $\sigma_b$  at the Gamow peak, that is, the quantity of interest for astrophysics.

In fact, nuclear reaction cross sections measured in the laboratory exhibit an enhancement of their values, with respect the bare nucleus ones, given by [6]

$$f_{\text{enh}} = \frac{\sigma_{\text{sh}}}{\sigma_b} \approx \exp\left(\pi\eta\frac{U_e}{E}\right), \quad (1)$$

$\sigma_{\text{sh}}$  being the shielded nuclear cross section measured in the laboratory,  $\sigma_b$  the bare-nucleus cross section,  $\eta$  the Sommerfeld parameter [6] and  $U_e$  the electron screening potential in the laboratory. The combined effects of Coulomb barrier penetration and electron screening make it difficult to access the Gamow energy window, leaving extrapolation as the most common way to extract the  $S(E)$ -factor:

$$S(E) = E\sigma(E)\exp(2\pi\eta) \quad (2)$$

down to the relevant energies.

To reduce these uncertainties, several indirect methods have been developed in the last few years in order to access the energy region of interest for astrophysics without the need of extrapolations. In particular, the Trojan horse method (THM) has provided a valid alternative approach to measure the bare nucleus  $S(E)$ -factor of charged-particle induced reactions at the Gamow peak, free from Coulomb suppression and electron screening effects [9–25].

This paper reports on a new investigation of this reaction by means of the THM applied to the  ${}^2\text{H}({}^{11}\text{B},\alpha_0){}^8\text{Be}$  reaction. This work was also motivated by the renewed interest for the  ${}^{11}\text{B}+\text{p}$  interaction as one of the most promising candidates as clean fuel for the aneutronic fusion in future fusion power plants. The range of energies for the  ${}^{11}\text{B}+\text{p}$  fuel cycle perfectly overlaps with that of LiBeB stellar burning. In the first part of the paper, a short review of previous  ${}^{11}\text{B}(\text{p},\alpha){}^8\text{Be}$  experimental studies is presented. Then, after a summary of the basic features of the THM, the new experimental study is described together with the analysis followed to extract the astrophysical  $S(E)$ -factor and the electron screening potential  $U_e$ . The obtained results are then discussed and compared with those extracted from previous measurements.

## 2. The ${}^{11}\text{B}(\text{p},\alpha){}^8\text{Be}$ reaction: status of the art

Several direct measurements were performed to study the  ${}^{11}\text{B}(\text{p},\alpha){}^8\text{Be}$  reaction.

Summarizing the main results, the low-energy behavior of the astrophysical  $S(E)$  factor is dominated by a resonant state at about  $\sim$ 600 keV in the  ${}^{11}\text{B}$ -p center of mass system, corresponding to the 16.57 MeV ( $J^\pi = 2^-$ ) level of  ${}^{12}\text{C}$ , and by an additional further low-energy resonance at about  $\sim$ 150 keV, corresponding to the 16.106 MeV ( $J^\pi = +$ ) level of  ${}^{12}\text{C}$ . In particular, in the case of  ${}^{11}\text{B}(\text{p},\alpha_0){}^8\text{Be}$  ( $Q = 8.59$  MeV) the  $S(E)$ -factor shows the presence of the  $l = 1$   $\sim$ 150 keV peak superimposed onto a nonresonant contribution while the  $\sim$ 600 keV level cannot contribute to the  $\alpha_0$  yield due to its  $J^\pi$  value of  $2^-$ . In the case of  ${}^{11}\text{B}(\text{p},\alpha_1){}^8\text{Be}^*$  ( $Q = 5.56$  MeV), both levels contribute to the  $\alpha_1$  reaction yield.

In particular, the direct measurements of the  ${}^{11}\text{B}(\text{p},\alpha){}^8\text{Be}$  reaction cross section at the energetic window relevant for astrophysics are given in [26–29]. In [26], several states of  ${}^{12}\text{C}$  are studied and a complete evaluation of angular distributions for emitted  $\alpha$ -particles for both  $\alpha_0$  and  $\alpha_1$  channels is reported in the energy range between  $0.5 < E_p < 4$  MeV, with  $E_p$  the bombarding proton energy measured in the laboratory system. In [27], the authors report

on the measurement of the reaction cross section for proton bombarding energy between  $35.4 < E_p < 1500$  keV. Angular distributions for both  $\alpha_0$  and  $\alpha_1$  channels are measured, with an evaluation of the natural width of the  $\sim 150$  keV level in the  $^{11}\text{B-p}$  system of  $\Gamma = 5.2^{+0.5}_{-0.3}$  keV. In [28], the authors report on the investigation of both  $\alpha_0$  and  $\alpha_1$  channels. In particular, to investigate the contribution of the resonant level at about 150 keV in the  $^{11}\text{B-p}$  center of mass, an evaluation of the excitation function with both solid and gas targets is performed. However, in this work, no evaluation of the electron screening effect is present and the *extrapolated* astrophysical  $S(E)$ -factor values are  $S(0) = 2.1$  MeV b ( $\alpha_0$ ) and  $S(0) = 195$  MeV b ( $\alpha_1$ ) (as given in [28]). The authors give a total  $S(E)$ -factor of  $197 \pm 12$  MeV b.

A further investigation of the total  $S(E)$ -factor ( $\alpha_0$  and  $\alpha_1$  channels together) is discussed in [29]. In this work, the  $S(E)$ -factor is measured from  $E_{\text{cm}} = 132$  keV down to  $E_{\text{cm}} = 18.73$  keV to extract the experimental value of the electron screening potential. From such a measurement, they quote an electron screening potential of  $U_e = 430 \pm 80$  eV. Such a value is higher than the upper limit provided by the adiabatic model,  $U_e^{\text{ad}} = 340$  eV [29], confirming the systematic discrepancy between experimental and theoretical values for the electron screening potential (see [7, 8] and references therein). These direct measurements [26–29] are also included in the NACRE compilation for nuclear astrophysics [30].

Although direct measurements of the  $^{11}\text{B(p,}\alpha)^8\text{Be}$  reaction span a wide range of energies, the present value of the astrophysical  $S(E)$ -factor at energies relevant for astrophysics and the electron screening potential are derived from extrapolations of high-energy direct data.

The indirect study of the  $^{11}\text{B(p,}\alpha)^8\text{Be}$  via the THM allows one to measure the astrophysical  $S(E)$ -factor even in the *extrapolation* energy region relevant for astrophysics, where both Coulomb suppression [18] and electron screening effects are dominant. In [31], a detailed analysis of a first THM investigation of the  $^{11}\text{B(p,}\alpha_0)^8\text{Be}$  is reported. The possibility of extracting the astrophysical  $S(E)$ -factor for such a reaction by properly selecting the quasi-free (QF) contribution to the  $^2\text{H}(^{11}\text{B,}\alpha_0^8\text{Be})\text{n}$  reaction induced at a  $^{11}\text{B}$  bombarding energy of 27 MeV has been underlined there. This work represents a further validation of the THM at very low energies [13], thanks to the possibility of studying the  $\sim 150$  keV level in the  $^{11}\text{B(p,}\alpha_0)^8\text{Be}$ . However, due to the poor experimental resolution of the whole set of experimental data discussed in [31], it was possible to extract the  $^{11}\text{B(p,}\alpha_0)^8\text{Be}$   $S(E)$ -factor by showing the resonant  $\sim 150$  keV peak with a FWHM of about 140 keV, larger than the one reported in the literature. Nonetheless, this result represents a very important validity test of the THM as it shows the possibility of investigating low-energy resonances, with the  $\sim 150$  keV level well below the  $^{11}\text{B-p}$  Coulomb barrier ( $\sim 1.7$  MeV). The previous zero-energy  $S(E)$  factor estimate was  $S(0) = 0.41 \pm 0.09$  MeV b [31]. Because the extracted bare nucleus  $S(0)$  was smaller than the only one available from the direct measurement of [28], a further study has been suggested in the same reference. Starting from the discrepancy between direct and TH data and taking advantage of the larger improvements made in the last few years in data analysis techniques, an analysis of the same experimental data was later performed. In particular, in [32, 33], the determination of the  $S(E)$ -factor for the  $^{11}\text{B(p,}\alpha_0)^8\text{Be}$  reaction is reported by selecting only the experimental conditions corresponding to the best  $^{11}\text{B-p}$  energy resolution in the center of the mass system, for which the resonant peak shows a FWHM of  $\sim 95$  keV. The obtained value in that preliminary re-analysis was  $S(0) = 2.2 \pm 0.3$  MeV b, in agreement with the direct data of [28]. The result extracted in [32, 33] refers only to part of the whole experimental data discussed in [31], i.e. those corresponding to a very small  $\theta_{\text{cm}}$  angular range and with an energy resolution of about  $\sim 95$  keV (FWHM).

In this work, we report on a new experiment, aiming to confirm the result obtained in [32, 33] and to investigate the behavior of the THM  $S(E)$ -factor in another center of mass

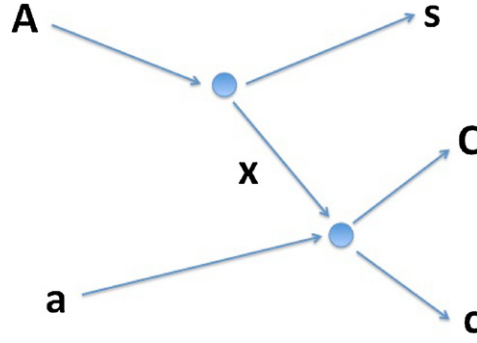


**Figure 1.** Pole diagram describing the QF  $a + A \rightarrow c + C + s$  reaction discussed in the text. Nucleus  $A$  breaks up into fragments  $x$  and  $s$ . The former is the *participant* of the binary reaction  $a(x, c)C$ , while the *spectator*  $s$  does not take part to the reaction.

angular range, for which an improved data analysis technique has been developed, and on its application to the data of [32, 33].

### 3. The THM: basic theory

The THM selects the QF contribution of an appropriate  $2 \rightarrow 3$  reaction  $a + A \rightarrow c + C + s$  [34, 35], performed at energies well above the Coulomb barrier. This allows one to extract the cross section for a charged-particle-induced  $a + x \rightarrow c + C$  reaction at astrophysical energies free of Coulomb suppression [18]. The THM has its scientific background in the theory of direct reaction mechanisms, and in particular in the studies of the QF reaction mechanisms [35]. The application to the nuclear astrophysics is an extension of the measurements of the excitation function from three-body QF reactions to low energies [36–38]. In particular, the THM has been successfully applied to determine the bare nucleus cross section for charged-particle-induced reactions at sub-Coulomb energies (see [9, 11–14, 16–25, 35]). In this paper, the THM will be presented within the plane wave impulse approximation (PWIA) framework, while more sophisticated theoretical formulations can be found in [34, 39–42].

The QF  $a + A \rightarrow c + C + s$  reaction between the projectile  $a$  and the target  $A$ , whose wavefunction is assumed to have a large amplitude for the  $A = x \oplus s$  cluster configuration, can be described by figure 1 [43–45]. It represents the dominant process (pole approximation), while other processes, such as re-scattering between the reaction products, are neglected [44]. In this framework, the projectile  $a$  interacts only with a part ( $x$ -cluster) of the target nucleus  $A$ , while the other part ( $s$ -cluster) is considered as the *spectator* to the  $a(x, c)C$  virtual reaction. In the impulse approximation (IA), the  $a(A, c)C$  reaction cross section is proportional to the  $a + x \rightarrow c + C$  cross section [46]. Following the simple PWIA, the three-body reaction can be factorized into two terms corresponding to the vertices of figure 1 and it is given by [47, 48]

$$\frac{d^3\sigma}{dE_c d\Omega_c d\Omega_C} \propto \text{KF} \cdot |\Phi(\vec{p}_s)|^2 \cdot \left( \frac{d\sigma}{d\Omega} \right) \Big|_{a-x}^{\text{HOES}} \quad (3)$$

where

- (i) KF is a kinematical factor containing the final state phase space factor and is a function of the masses, momenta and angles of the outgoing particles [49, 50];
- (ii)  $\Phi(\vec{p}_s)$  is the Fourier transform of the radial wavefunction for the  $\chi(r_{xs}^{\vec{r}})$  inter-cluster motion usually described in terms of Hänkel, Eckart or Hulthén functions depending on the  $x$ - $s$  system (see [55–57] and references therein);

(iii)  $(d\sigma/d\Omega)_{a-x}^{\text{HOES}}$  is the half-off-energy-shell (HOES) differential cross section for the binary  $a(x, c)C$  reaction ([41] and references therein). It is induced at the center of mass energy  $E_{\text{cm}}$  given in post-collision prescription (PCP) by the relation  $E_{\text{cm}} = E_{cC} - Q_{2b}$  [51], where  $Q_{2b}$  is the  $Q$ -value for the binary  $a + x \rightarrow c + C$  reaction and  $E_{cC}$  is the relative energy in the exit channel between particle  $c$  and  $C$ .

In the applications of the THM, the  $x$ - $s$  cluster system in the nucleus  $A$  is most likely in the  $s$ -state; thus, the expected momentum distribution has a maximum at  $p_{xs} = 0$  MeV/ $c$ .

### 3.1. Energy and momentum prescriptions

QF processes have been applied in the past for studying  $2 \rightarrow 3$  reactions, induced on light nuclei at low energy, with high  $Q$ -value thus allowing one to detect the QF effects in correspondence of high momenta ( $\geq 300$  MeV/ $c$ ) in the exit channel [50]. The beam energy is chosen in such a way to overcome the Coulomb barrier in the entry channel  $a + A$ . Thus, particle  $x$  is brought inside the nuclear interaction zone to induce the relevant reaction  $a + x \rightarrow c + C$ . The QF kinematical conditions must be chosen in such a way that the relative energy  $E_{a-x}$  can span the astrophysical region of interest below the Coulomb barrier in the channel  $a - x$  [34]. This is possible because the initial projectile velocity is compensated for by the binding energy of particle  $x$  inside  $A$  ([9, 31, 50] and references therein). Thus, the  $a - x$  relative energy of the fragments can be very low. In symbols, we have

$$E = E_{a-x} - B_{xs} = E_{\text{QF}} \quad (4)$$

with  $E_{a-x}$  the projectile energy in the two-body center of mass system and  $B_{xs}$  the  $x - s$  binding energy. It is very important to experimentally validate the correctness of the pole approximation in each specific case [43–45]. The applicability of the pole approximation is limited to the small momentum  $p_s$  with a prescription given by [43–45]:

$$0 \leq p_s \leq k_{xs} \quad (5)$$

with  $p_s$  the HOES momentum of the cluster  $x$  when it interacts with the particle  $a$ , and  $k_{xs}$  defined by the relation  $k_{xs} = \sqrt{2\mu_{xs}B_{xs}}$ , being  $\mu_{xs}$  the  $x - s$  reduced mass.

### 3.2. Experimental momentum distribution in IA

Once the energy and momentum have been chosen in order to satisfy the prescriptions described above, it is necessary to determine, for each experiment, the experimental momentum distribution for the  $x$ - $s$  system via the QF  $2 \rightarrow 3$  reaction. If the cross section is known, the momentum distribution  $\Phi(\vec{p}_s)$  can be obtained from the QF yield with the energy sharing method or by measuring an angular correlation (see [50] and references therein). The momentum distribution  $\Phi(\vec{p}_s)$  is obtained, in the energy sharing approach, by selecting a narrow relative energy windows  $\Delta E_{\text{cm}}$  and center of mass angular range. If the factorization of equation (3) is applicable, dividing the QF coincidence yield ( $Y$ ) by the kinematic factor, a quantity which is proportional to the product of the momentum distribution by the  $a+x \rightarrow c+C$  cross section is obtained [31, 50]. In a restricted relative energy  $\Delta E_{\text{cm}}$  and center of mass angular range, the differential cross section can be considered almost constant and

$$|\Phi(\vec{p}_s)|^2 \propto \frac{Y}{\text{KF}}. \quad (6)$$

The procedure described above has been used for several reactions to measure the width (FWHM) of the experimental momentum distribution used in extracting the THM data via equation (3) [50].

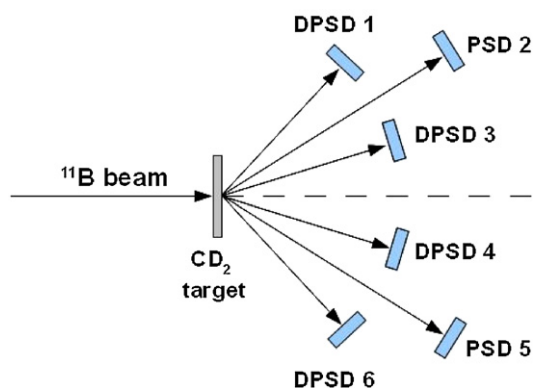


**Figure 2.** Sketch of the experimental setup discussed in the text. A 27 MeV  $^{11}\text{B}$  beam impinges on a  $\text{CD}_2 \sim 170 \mu\text{g cm}^{-2}$  thick target. The outgoing  $^8\text{Be}$  and  $\alpha$  particles were detected by means of DPSD and PSD detectors, respectively. The displacement of the setup inside the CAMERA 2000 scattering chamber was chosen in order to cover the QF angular range predicted by kinematical calculations.

Besides the PWIA approach, more sophisticated theoretical approaches have been developed over the years for describing QF reactions. In particular, the distorted wave impulse approximation (DWIA) [52, 53] or distorted wave Born approximation (DWBA) [40, 54] treatment have been sometimes applied in the analysis of QF reactions and QF scattering experimental data. It has been proved that the distortion effects are negligible for spectator momentum values lower than  $\sqrt{2\mu_{\alpha\text{B}}B_{\alpha\text{B}}}$  (for example,  $\sim 40 \text{ MeV}/c$  for the  $p$ - $n$  relative motion inside the deuteron) [20, 22, 23, 31, 56, 57]. The only significant change with respect to the PWIA in this momentum range is a decrease of the absolute value of the momentum distribution due to wave absorption effects, without affecting the shape of the momentum distribution itself. Though one cannot extract the absolute value of the two-body cross section, it can be obtained through normalization to the available direct data, thus compensating for the overestimate of the momentum distribution absolute value as deduced in the PWIA approach [31, 56, 57].

#### 4. The experiment

The  $^2\text{H}(^{11}\text{B},\alpha^8\text{Be})n$  experiment was performed at Laboratori Nazionali del Sud of Catania using  $^2\text{H}$  as the ‘TH-nucleus’. Deuteron represents one of the most suitable TH-nuclei, together with  $^6\text{Li}$  or  $^3\text{He}$ , thanks to its obvious  $p \oplus n$  cluster structure and to a well-known radial wavefunction described in terms of a Hulthén function ([38] and references therein). The experiment was performed to make an improvement to the previous experimental study of the  $^{11}\text{B}(p,\alpha_0)^8\text{Be}$  [31], the  $\alpha_0$  channel implying the study of the alpha-particles leaving the beryllium in its ground state ( $E_{\text{g.s.}} = 91.84 \pm 0.04 \text{ keV}$ ,  $\tau = 10^{-18} \text{ s}$  [59]), and then to extract the low energy  $S(E)$ -factor in correspondence to the astrophysically relevant energy range.

The detection setup (sketched in figure 2) was then thought of and designed for detecting both outgoing particles,  $\alpha$  and  $^8\text{Be}$ , with the ‘event’  $^8\text{Be}$  reconstructed following the same experimental procedure adopted in [31]. In more detail, the setup consisted of four dual position sensitive detectors (DPSD), made of two  $50 \times 10 \text{ mm}^2$  position sensitive silicon detectors (PSD) mounted one above the other and separated by an empty 1 mm space. They were dedicated to the coincident detection of the two alphas from the ground state of  $^8\text{Be}$ . Two

PSDs were further used with the aim to detect the other alpha-particles in the exit channel. All the DPSDs were placed symmetrically with respect to the beam line direction at about 200 mm from the target. The two PSDs were placed 300 mm from the target. In particular, DPSD1 covered  $47^\circ \pm 7^\circ$ , PSD2  $32^\circ \pm 5^\circ$  and DPSD3  $17^\circ \pm 7^\circ$  with respect to the beam line. Detectors DPSD6, PSD5 and DPSD4 were placed at the same angles respectively but on the other side with respect to the beam line direction. The correct planarity of the three detectors was checked by an optical system. The SMP Tandem Van de Graaf accelerator provided a 27 MeV  $^{11}\text{B}$  beam with a spot size on target of about 1.5 mm with an energy spread of about  $10^{-4}$ , and intensities ranging between 2 enA and 4 enA. A self-supported  $170 \mu\text{g cm}^{-2}$  thick deuterated polyethylene target ( $\text{CD}_2$ ) was placed at  $90^\circ$  with respect to the beam direction. The high energy in the  $^{11}\text{B}-^2\text{H}$  center of mass system,  $E_{\text{cm}}^{\text{beam}} = 4.15 \text{ MeV}$ , allows us to overcome the Coulomb barrier  $E_{\text{Coul.}} \approx 1.6 \text{ MeV}$  in the entrance channel of the  $^2\text{H}(^{11}\text{B}, \alpha^8\text{Be})\text{n}$  reaction. The displacement of the detection setup was chosen in order to cover the region at which a strong contribution of the QF mechanism is expected and to cover momentum values of the *undetected* neutron between 0 and  $\sim 200 \text{ MeV}/c$ . This ensures that the bulk of the QF contributions for the breakup process of interest falls inside the investigated regions, because the momentum distribution for the  $p-n$  system has a maximum at  $p_s = 0 \text{ MeV}/c$ . The angles corresponding to this condition are known as *QF angles*. The displacement of the detection setup allowed one to cross check the method inside and outside the regions where the QF contribution is expected.

Energy and position signals of the detected particles were processed by standard electronics and sent to the acquisition system for online monitoring of the experiment and data storage. The trigger of the acquisition was generated by events having particle multiplicity larger than 1.

## 5. Data analysis

### 5.1. Detector calibration

For the angular calibration, an equally spaced grid was mounted in front of each detector and the angular position of each grid inside the scattering chamber was determined by using an optical system. The position and energy calibrations were then performed delivering a 9 MeV  $^6\text{Li}$  beam on gold ( $^{197}\text{Au}$ ), carbon ( $^{12}\text{C}$ ) and deuterated polyethylene ( $\text{CD}_2$ ) target to use the kinematics of the elastic scattering  $^6\text{Li} + ^{197}\text{Au}$  and  $^6\text{Li} + ^{12}\text{C}$  as well as the  $^6\text{Li} + ^{12}\text{C} \rightarrow \alpha + ^{14}\text{N}$  reaction. For the calibration at the low-energy region, a standard 3-peak alpha-source ( $^{241}\text{Am}$ ,  $^{244}\text{Cm}$ ,  $^{239}\text{Pu}$ ) was used. The calibration procedure leads to an energy determination better than 1% and an angular determination better than  $0.3^\circ$  for each silicon detector.

### 5.2. Identification of $^8\text{Be}$ events

After the detector calibration, the selection of the  $2 \rightarrow 3 \text{ } ^2\text{H}(^{11}\text{B}, \alpha^8\text{Be})\text{n}$  reaction channel was performed. For this purpose, the first stage was the reconstruction of the ‘events’  $^8\text{Be}_{\text{g.s.}}$  as a coincidence between the upper and lower part of the DPSD array, as already discussed in [31]. In more detail, the relative energy between two particles hitting such detectors in coincidence was easily reconstructed by means of the standard formula

$$E_{\alpha-\alpha} = \frac{1}{2} \mu v_{\alpha-\alpha}^2 \quad (7)$$

with  $\mu$  the reduced mass of the two particles and  $v_{\alpha-\alpha}^2 = (\mathbf{v}_1 - \mathbf{v}_2) \cdot (\mathbf{v}_1 - \mathbf{v}_2)$  the square of their relative velocity. By measuring the energy and position of each particle, it was possible to extract its correspondence velocity. By assuming a mass 4 for those particles, the

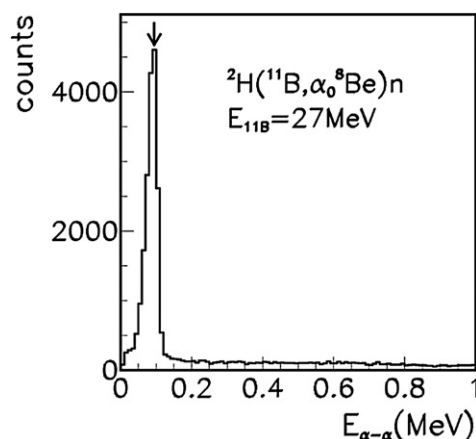


**Figure 3.** Typical alpha-alpha relative energy spectrum from the coincident detection of two particles in a DPSD. The pronounced peak around 90 keV is a signature of the two alpha decay from  ${}^8\text{Be}_{\text{g.s.}}$ .

obtained experimental spectrum is shown in figure 3, where the prominent peak is due to the  ${}^8\text{Be}_{\text{g.s.}} \rightarrow \alpha + \alpha$  events. By fitting the experimental spectrum, a value of  $E_{\alpha-\alpha} = 91.17 \pm 0.03$  keV and a width of  $\sim 33$  keV have been obtained. The measured  $E_{\alpha-\alpha}$  deviates by  $\sim 0.7\%$  from the tabulated one, namely 91.84 keV [59], giving an estimate of the systematic uncertainties due to energy and angular calibration. The selection of events involving a  ${}^8\text{Be}$  nucleus in its ground state was performed by gating on this 90 keV peak. This procedure allowed one to ‘reconstruct’ the energy  $E_{\text{Be}}$  and angle  $\theta_{\text{Be}}$  of  ${}^8\text{Be}_{\text{g.s.}}$  from the measurement of energies and angles of two  $\alpha$  particles. After this stage, only these selected events were taken into account in the further data analysis.

### 5.3. Selection of the ${}^2\text{H}({}^{11}\text{B}, \alpha_0 {}^8\text{Be})n$ reaction channel

To accomplish the selection of the  $2 \rightarrow 3$  channel, the  $Q$ -value of the  ${}^2\text{H}({}^{11}\text{B}, \alpha_0 {}^8\text{Be})n$  reaction was reconstructed by means of the momentum and energy conservation. Because the  $Q_{3\text{body}}$  is independent from any other kinematic variable in the three-body exit channel, a bidimensional plot of the  $Q_{3\text{body}}$  as a function of the ‘reconstructed angle’ for the  ${}^8\text{Be}$  has been used to select the events coming from the  ${}^2\text{H}({}^{11}\text{B}, \alpha_0 {}^8\text{Be})n$  reaction. As shown in figure 4, the variable  $Q_{3\text{body}}$  does not depend on the  $\theta_{\text{Be}}$  as expected. For this reason, this 2D plot allows one to first check the quality of energy-position calibrations and second to check the angular range covered by the *reconstructed*  ${}^8\text{Be}$  events, which is in good agreement with the angular range predicted by the kinematic simulation. The experimental spectrum of the  $Q_{3\text{body}}$  for the  ${}^2\text{H}({}^{11}\text{B}, \alpha_0 {}^8\text{Be})n$  is shown in figure 5, for which a fitted value of  $6.351 \pm 0.002$  MeV (FWHM  $\sim 0.520$  MeV) was obtained in agreement with the theoretical 6.36 MeV one<sup>13</sup>. Only the events falling inside this peak will be considered for the next steps of data analysis. The locus of events  $E_\alpha$  versus  $E_{\text{Be}}$  for the  ${}^2\text{H}({}^{11}\text{B}, \alpha_0 {}^8\text{Be})n$  reaction was compared with the corresponding three-body kinematic calculation, appearing to be very well reconstructed. As an example, the experimental locus of events  $E_\alpha$  versus  $E_{\text{Be}}$  for  $\theta_\alpha = 52^\circ \pm 1^\circ$  and  $\theta_{\text{Be}} = 16^\circ \pm 1^\circ$  is shown in figure 6 as black points, while the red ones represent the 2D simulation in the same angular condition. Such a

<sup>13</sup> <http://t2.lanl.gov/>

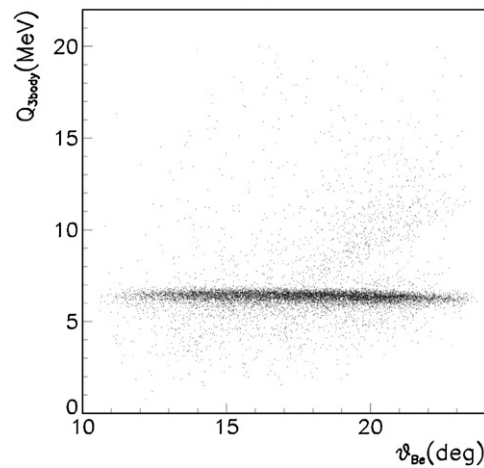


**Figure 4.**  $Q_{3\text{body}}$  versus  $\theta_{\text{Be}}$ : the horizontal line at about 6.4 MeV strongly suggests the presence of events coming from the  ${}^2\text{H}({}^{11}\text{B}, \alpha_0 {}^8\text{Be})\text{n}$  reaction channel.

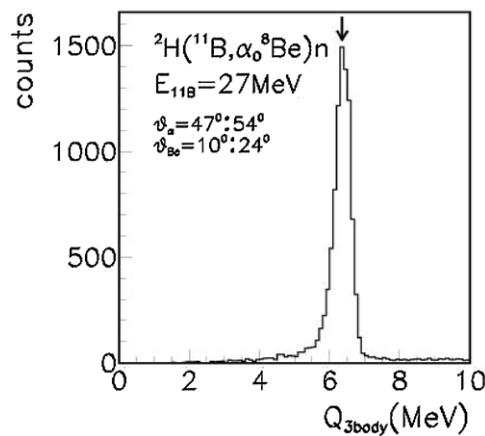


**Figure 5.** Experimental  $Q$ -value for the  ${}^2\text{H}({}^{11}\text{B}, \alpha_0 {}^8\text{Be})\text{n}$  reaction peaked at  $\sim 6.4$  MeV.

comparison strongly confirms the goodness of the adopted calibration and the correct selection of the reaction channel of interest.

#### 5.4. Selection of the QF reaction mechanism

The next step of a typical TH data analysis is the evaluation of the reaction mechanisms leading to the population of the  $\alpha+{}^8\text{Be}+\text{n}$  exit channel. Their production can in fact be due to both QF and sequential mechanisms (SM), i.e. possible formation/de-excitation of intermediate compound nucleus states. To evaluate the contribution of such ‘competing’ SM, the relative energies between the outgoing particles were then reconstructed. In particular, the study of a two-dimensional plot of any two of the  $E_{\alpha-\text{Be}}$ ,  $E_{\alpha-\text{n}}$  and  $E_{\text{Be}-\text{n}}$  relative energies allows one to obtain information on the presence of excited states of  ${}^{12}\text{C}$ ,  ${}^5\text{He}$  and  ${}^9\text{Be}$ , respectively. From these plots shown in figure 7, the clear vertical locus in both upper and lower panels is

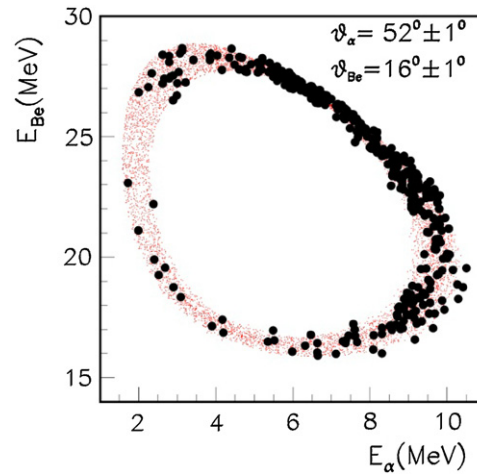


**Figure 6.** Experimental kinematical locus (black points) superimposed to the simulation (red points) once the angular condition  $\theta_\alpha = 52^\circ \pm 1^\circ$  and  $\theta_{Be} = 16^\circ \pm 1^\circ$  has been fixed.

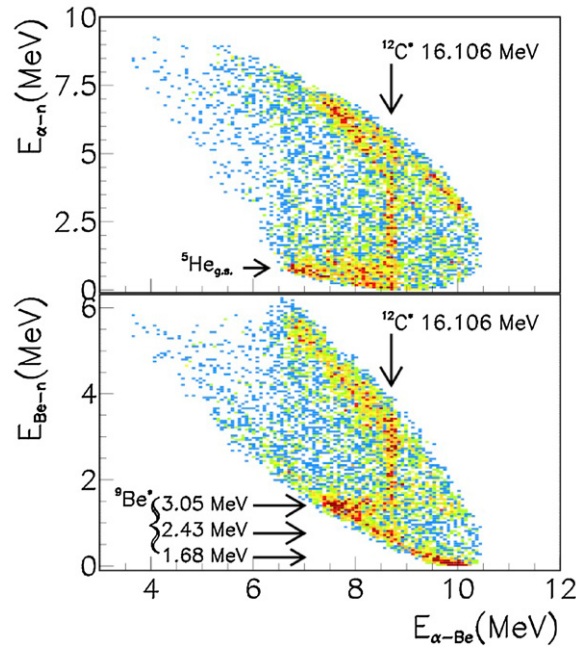


**Figure 7.** Bi-dimensional plot of  $E_{\alpha-n}$  and  $E_{Be-n}$  relative energies as a function of  $E_{\alpha-Be}$ . The vertical arrows indicate the position of the 16.106 MeV  $^{12}C^*$  excited level, while the horizontal ones mark the position of  $^5He$  and  $^9Be$  levels in the upper and lower panels, respectively.

related to the 16.106 MeV  $^{12}C$  level ( $J^\pi = 2^+$  [58]), corresponding in this case to an  $\alpha$ -Be relative energy of about  $E_{\alpha-Be} \sim 8.7$  MeV. In particular, the 16.106 MeV is just above the  $^{11}B$ -p threshold, thus implying its relevance for THM application. Moreover, events coming from the de-excitation of the 1.68 MeV ( $J^\pi = \frac{1}{2}^+$ ), 2.43 MeV ( $J^\pi = \frac{5}{2}^-$ ) and 3.05 MeV

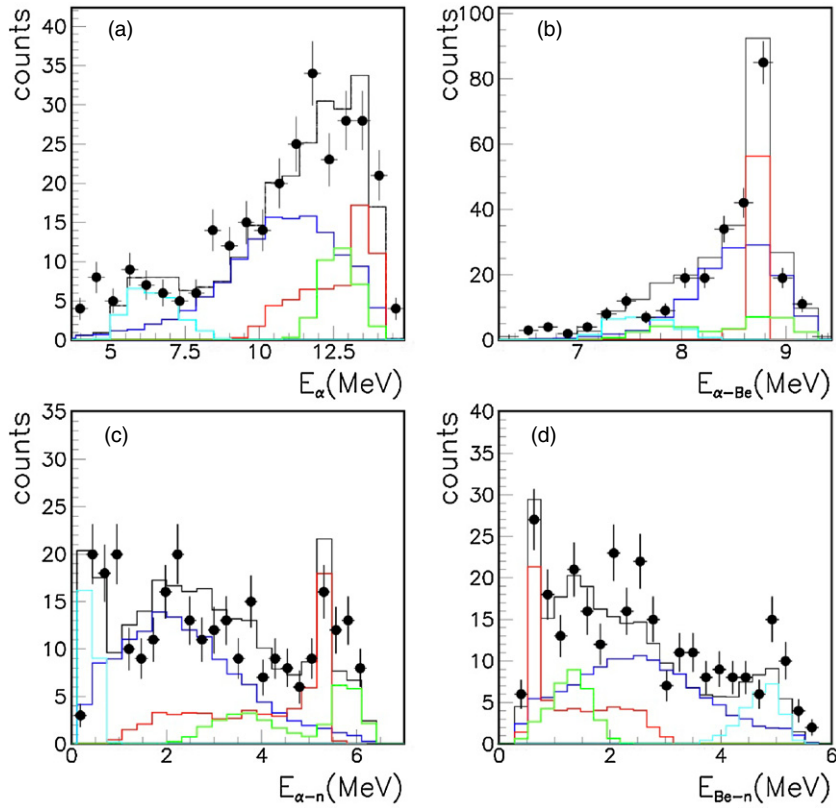


**Figure 8.** Typical coincidence spectra (black points) projected on  $E_\alpha$ ,  $E_{\alpha-\text{Be}}$ ,  $E_{\alpha-n}$  and  $E_{\text{Be}-n}$  for the QF angular pair  $\theta_\alpha = 45^\circ \pm 1^\circ$  and  $\theta_{\text{Be}} = 20^\circ \pm 1^\circ$ . (a) The full histogram represents the simulated spectrum in the  $E_\alpha$  variable obtained as the incoherent sum of the QF contribution from direct break-up (blue histogram), and of the  $^{12}\text{C}$  (red histogram),  $^9\text{Be}$  (green histogram) and the  $^5\text{He}_{\text{g.s.}}$  (aqua histogram) resonances cited in the text. (b)–(d) Data are represented as a function of the other variables.

$(J^\pi = \frac{5}{2}^+)$   $^9\text{Be}$  levels give a contribution as diagonal loci in the top panel of figure 7 or as horizontal ones in the bottom of the same figure. A contribution from  $^5\text{He}_{\text{g.s.}}$  decay can also be recognized. These events represent a background and their contribution must be reduced as much as possible, before applying the THM.

A quantitative analysis of the presence of SM and QF mechanisms was performed by studying the coincidence yield of the three-body reaction projected onto different variables for fixed values of  $\theta_\alpha$  and  $\theta_{\text{Be}}$ . The spectra were then compared with simulated spectra obtained by incoherently adding the contributions of SM and QF reactions. In particular, the coincidence yields for SM were described assuming a Breit–Wigner shape for the spreading of the  $^{12}\text{C}$ ,  $^5\text{He}$  and  $^9\text{Be}$  levels feeding in the three-body exit channel, while the QF process was described by equation (3). For each fixed pair ( $\theta_\alpha$  and  $\theta_{\text{Be}}$ ), the simulated spectra were firstly calculated for the  $E_\alpha$  spectrum, and the obtained weights for the different SM and QF processes were used to reproduce the  $E_{\alpha-\text{Be}}$ ,  $E_{\alpha-n}$  and  $E_{\text{Be}-n}$  spectra. Typical spectra are shown in figure 8 for the QF angular pair  $\theta_\alpha = 45^\circ \pm 1^\circ$  and  $\theta_{\text{Be}} = 20^\circ \pm 1^\circ$ . In particular, figure 8(a) shows the experimental  $E_\alpha$  spectrum compared with the simulated

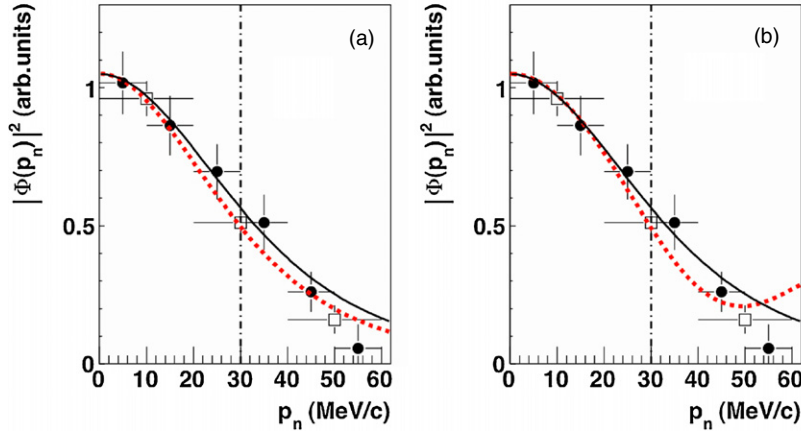


**Figure 9.** (a) The experimental momentum distribution (full circles and open squares) with their fit (black solid line) compared with the square of the theoretical Hulthén function, in momentum space, in the PWIA (red dashed line). (b) The same experimental momentum distribution (full circles and open squares) with their fit (black solid line) compared with the DWBA momentum distribution evaluated using the FRESKO code (red dashed line). The vertical dot-dashed lines, in both panels, mark the position of the strict selection on the experimental data needed for the TH application (see the text and [50]).

one (black histogram) given as the incoherent sum of the QF contribution from the direct break-up (blue histogram) and of the  $^{12}\text{C}$  (red histogram),  $^9\text{Be}$  (green histogram) and the  $^5\text{He}_{\text{g.s.}}$  (aqua histogram) resonances cited above. The same weights were then used to generate the black histograms plotted in figures 8(b)–(d) and compared with the experimental spectra on the variables  $E_{\alpha-\text{Be}}$ ,  $E_{\alpha-n}$  and  $E_{\text{Be}-n}$ . This procedure results in a QF contribution on the coincidence yield ranging from  $\sim 20\%$  up to  $\sim 75\%$  in correspondence to the QF angles. To reduce the contribution of SM from  $^5\text{He}_{\text{g.s.}}$  and  $^9\text{Be}$ , contributing to the coincidence yield up to a maximum of  $\sim 80\%$ , only the events corresponding to  $E_{\alpha-n} > 1$  MeV (see figure 8(c)) and  $E_{\text{Be}-n} > 2$  MeV (see figure 8(d)) were taken into account in the further steps of the data analysis.

After this analysis, the selection of events from the QF mechanism was performed. An unambiguous signature of the QF mechanism is provided by the shape analysis of the momentum distribution of the undetected third particle in the exit channel. In the QF hypothesis, the neutron in the exit channel should maintain its momentum distribution as inside the deuteron before the interaction with the impinging particle takes place. By selecting a small energy region where the two-body cross section is assumed to be constant, the three-body coincidence yield divided by KF is proportional to the momentum distribution  $|\Phi(\vec{p}_n)|^2$ , as already discussed in subsection 3.2.

A typical experimental result is shown in figure 9(a), where the coincidence yield for the events in the energy window  $E_{\text{cm}} = 0.15 \pm 0.05$  MeV divided by the phase-space factor is shown (black points). The error bars include only the statistical one.

An alternative experimental method for the extraction of the experimental momentum distribution was adopted in this work. In particular, three different experimental spectra for the variable  $E_{\text{cm}} = E_{\alpha-\text{Be}} - 8.59$  MeV have been extracted. Each spectrum has been produced with a different selection on the neutron momentum values, i.e.  $10 \pm 10$  MeV/c,  $30 \pm 10$  MeV/c and  $50 \pm 10$  MeV/c. A selection on the center of mass angle  $\theta_{\text{cm}} = 65^\circ \pm 15^\circ$  was

also applied. For each spectrum, the area below the resonant contribution has been evaluated and plotted as a function of the neutron momentum values. The results obtained with this alternative approach are shown in figure 9(a) as open squares.

The experimental momentum distribution extracted here has a width of  $65 \pm 10$  MeV/ $c$  (FWHM) (black solid line in figure 9(a)). This was then compared with the theoretical one, given in terms of a Hulthén wavefunction in momentum space:

$$\Phi(\vec{p}_n) = \frac{1}{\pi} \sqrt{\frac{ab(a+b)}{(a-b)^2}} \left[ \frac{1}{a^2 + p_n^2} - \frac{1}{b^2 + p_n^2} \right] \quad (8)$$

with standard parameters  $a = 0.2317$  fm $^{-1}$  and  $b = 1.202$  fm $^{-1}$  [38] for which the theoretical FWHM value is 58 MeV/ $c$  [11, 38, 56, 57] (figure 9(a), red dashed line). The good agreement, within the experimental errors, between the experimental data and the theoretical functions for the  $p$ - $n$  motion inside the deuteron represents the experimental evidence that the neutron acted as a ‘spectator’ during the break-up that occurred in the  ${}^2\text{H}({}^{11}\text{B}, \alpha_0^8\text{Be})n$  reaction. These results are also in agreement with the conclusion of [56, 57] for which, the high transferred momentum  $q_t \approx 370$  MeV/ $c$  reached in the present experiment, justifies a match between the experimental FWHM extracted here and its theoretical asymptotic value (see [56, 57, 50] for more details).

To check if the simple PWIA approach gives an accurate description of the  $p$ - $n$  momentum distribution, the experimental data and their fit were also compared with the DWBA distribution (red dashed line in figure 9(b)), which is evaluated by means of the FRESCO code [61]. In the calculation, optical potential parameters adjusted from the Perey and Perey compilation [62] were adopted. From the comparison in figure 9(b), we can state that a good agreement between DWBA and PWIA is present, within the experimental uncertainties, for neutron momentum values lower than 40 MeV/ $c$ . In particular, the vertical dot–dashed lines in both panels of figure 9 mark the position of the selected events for which the TH will be applied, i.e. only those events for which the neutron momentum values satisfy the condition previously described. The experimental TH data show that if the event selection is limited to the region close to the maximum of the momentum distribution, DWBA and PWIA approaches give the same results [20, 22, 23, 50]. This demonstrates that the PWIA approach provides a viable method to proceed further in the analysis for extracting the  $S(E)$  factor of our interest. The result obtained in the present experiment is firstly in agreement with the experimental value of the FWHM given in [31] and strongly corroborates the conclusions given in [56, 57], thus confirming once again the PWIA hypothesis.

## 6. Study of the astrophysically relevant reaction

As mentioned, the THM is based on the nuclear reaction theory developed for the QF reaction processes. Thus, its application proceeds through the selection of the events corresponding to the kinematical conditions where the QF mechanism is dominant. By following the energy and momentum prescriptions deeply discussed in [44, 45, 50] for the validity of the IA approach, only the experimental data corresponding to low momentum values of the undetected *spectator* were selected. In particular, only the experimental data of the  ${}^2\text{H}({}^{11}\text{B}, \alpha_0^8\text{Be})n$  reaction corresponding to the  $0 < p_n < 30$  MeV/ $c$  range were taken into account for the next steps of the analysis, respecting the prescriptions given in equation (5). The narrow range on the neutron momentum values, shown in both panels of figure 9 as a vertical dot–dashed line,

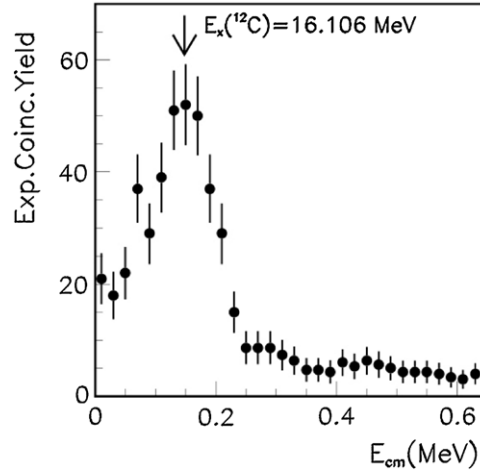


**Figure 10.** Experimental coincidence yield for the selected data. The well-separated peak at about 150 keV is due to the population of the 16.106 MeV  $^{12}\text{C}$  level.

guarantees, with high probability, the occurrence of the QF mechanism and the applicability of the IA formalism [44, 45, 50].

The selected  $2 \rightarrow 3$  coincidence yield is shown in figure 10 as a function of the variable  $E_{\text{cm}}$ . Clear evidence of a well-separated peak at about 150 keV is present together with a nonresonant contribution. By using standard error propagation, it was also possible to estimate an average experimental resolution of about 100 keV (FWHM) on the  $E_{\text{cm}}$  variable. Such experimental resolution justifies the present experimental width of the 150 keV level of about  $\sim 100$  keV, larger than its natural width,  $\Gamma = 5.2_{-0.3}^{+0.5}$  keV [58].

The experimental coincidence yield contains a nonresonant  $l = 0$  and a resonant  $l = 1$  contribution, required by the spin-parity conservation rule to populate the 16.106 MeV level of  $^{12}\text{C}$  from boron in its ground state ( $J^\pi = \frac{3}{2}^-$ ) and proton ( $J^\pi = \frac{1}{2}^+$ ).

### 6.1. Angular distributions

To compare the direct measurements with the TH data, the indirectly measured angular distributions were extracted as in [31]. The emission angle of the alpha-particle in the  $\alpha$ - $^8\text{Be}$  center of mass system can be calculated according to the relation [60]

$$\theta_{\text{cm}} = \arccos \frac{(\mathbf{v}_B - \mathbf{v}_p) \cdot (\mathbf{v}_{\text{Be}} - \mathbf{v}_\alpha)}{|\mathbf{v}_B - \mathbf{v}_p| |\mathbf{v}_{\text{Be}} - \mathbf{v}_\alpha|},$$

where the vectors  $\mathbf{v}_B$ ,  $\mathbf{v}_p$ ,  $\mathbf{v}_{\text{Be}}$ ,  $\mathbf{v}_\alpha$  are the velocities of projectile, transferred proton, and outgoing  $^8\text{Be}$  and  $\alpha$ -particles, respectively. These quantities can be calculated from their corresponding momenta in the lab system, where the momentum of the transferred particle is equal and opposite to that of the spectator neutron (QF assumption) [60]. The  $\theta_{\text{cm}}$  range covered in this experiment was from  $50^\circ$  to  $80^\circ$ . In the previous experiment, a  $\theta_{\text{cm}}$  range  $80^\circ$ – $120^\circ$  was also covered. A typical result corresponding to  $E_{\text{cm}} = 300 \pm 50$  keV is shown in figure 11, where the red points with their statistical errors refer to the experiment discussed in the text while the blue ones refer to the previous ones. The empty triangles are the direct data from [28] and the full line their fit as reported in [28]. The agreement between direct and indirect angular distributions allows us to integrate over the whole  $\theta_{\text{cm}}$  range and then

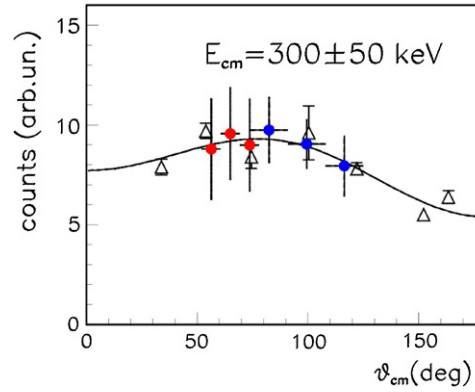


**Figure 11.** Experimental angular distributions at the energy  $E_{cm} = 300 \pm 50$  keV. The full dots are the THM data extracted from the experiment discussed in the text (red points) and those from a previous THM experiment (blue points). The error bars include only the statistical errors. The empty triangles are the direct data of [28] while the full line represents their fit by means of Legendre polynomials [28].

to proceed further for the extraction of the astrophysical  $S(E)$ -factor for the reaction under investigation.

## 6.2. Astrophysical $S(E)$ -factor

Selecting the experimental coincidence yield shown in figure 10 and calculating the product  $KF \cdot |\Phi(\vec{p}_s)|^2$  by means of a Monte Carlo simulation (in this case the spectator  $s$  is the neutron,  $s = n$ ), it is possible to extract the bare nucleus two-body cross section from equation (3):

$$\left(\frac{d\sigma}{d\Omega}\right)^{\text{HOES}} \propto \frac{d^3\sigma}{dE_\alpha d\Omega_{Be} d\Omega_\alpha} \cdot [KF \cdot |\Phi(\vec{p}_n)|^2]^{-1}, \quad (9)$$

which represents the half-of-energy shell two-body reaction cross section. Its experimental behavior is shown in figure 12 and it confirms the main difference between this quantity and the reaction cross section directly measured, i.e. the THM cross section does not suffer the exponential decrease of the cross section due to Coulomb barrier penetration. In detail, figure 12(a) displays the HOES cross section for the dataset whose analysis has been discussed in the previous sections while figure 12(b) shows the data from [32, 33] for which the same analysis procedure has been applied. Only statistical errors are displayed in both panels of figure 12, reaching a maximum value of  $\sim 40\%$  in (a) and a maximum value of  $\sim 20\%$  in (b).

Because this quantity represents only the nuclear part of the two-body reaction cross section [50], the penetrability through the Coulomb barrier has been introduced on the THM data in terms of  $F_l$  and  $G_l$  regular and irregular Coulomb functions [6] to compare the THM cross section (or the THM  $S(E)$ -factor) with the direct one.

As already mentioned, the ‘bare-nucleus’ THM cross-section  $\left(\frac{d\sigma}{d\Omega}\right)^N$  in figure 12 can be described as a resonant ( $l = 1$ ) superimposed onto a nonresonant ( $l = 0$ ) contribution. To disentangle the two different partial waves, a fit was performed for the two experimental data sets shown in figure 12 by using the incoherent sum of a second order polynomial and a Gauss function. The fit was performed with the sole aim of an evaluation of the two contributions on the selected experimental data. Once the non-resonant  $l = 0$  and the resonant

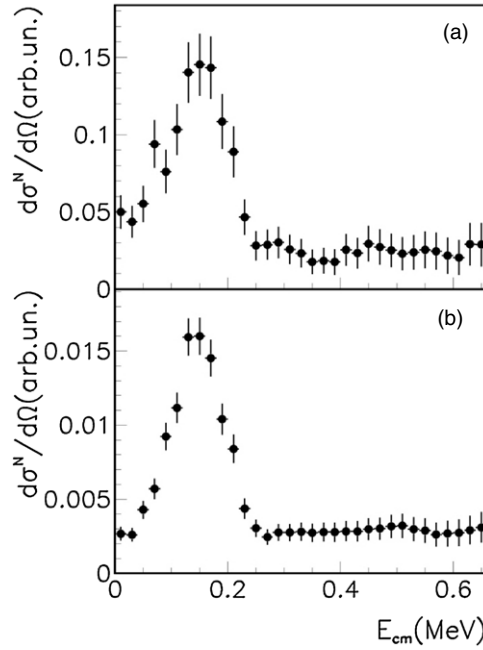


**Figure 12.** Nuclear part of the  $^{11}\text{B}(p, \alpha_0)^8\text{Be}$  reaction cross section. (a) The experimental data discussed in the text; (b) a past experiment (see the text for details).

$l = 1$  contributions have been evaluated, the penetrability through the Coulomb barrier was introduced with a cut-off radius  $R \approx 4.2$  fm [6].

For the next steps, a normalization procedure was needed, since the method, in its PWIA formulation, does not allow us to extract results in absolute units. To this aim, direct data from [28] were considered, together with the empirical fit of the astrophysical  $S(E)$ -factor for the  $^{11}\text{B}(p, \alpha_0)^8\text{Be}$  reaction. To take into account the energy resolution of the present experiment, a smearing procedure was necessary in order to describe the resonant contribution associated with the 150 keV resonant level. In such a procedure we required that the integral of the smeared function was the same of the function describing the empirical fit of [28]. The smeared function describing the direct data of [28] is given by

$$S(E)_{\alpha_0}^{\text{dir}}|_{\text{smear}} = 2.1 - 1.37E - 0.14E^2 + 7.99 \times \exp \left[ -0.5 \left( \frac{E - 0.148}{0.04} \right)^2 \right] \quad (10)$$

with the energy  $E$  in MeV and  $S(E)_{\alpha_0}^{\text{dir}}|_{\text{smear}}$  in MeV b. Such a function was then used for the normalization of the  $l = 0$  and  $l = 1$  contributions. The THM  $S(E)$ -factor for the  $^{11}\text{B}(p, \alpha_0)^8\text{Be}$  reaction was then obtained as the incoherent sum of the  $l = 0$  and the  $l = 1$  contribution after their normalization to the direct ‘smeared-out’ data. The  $l = 0$  contribution was normalized to the direct one in the energy region between  $E_{\text{cm}} = 400\text{--}600$  keV, while for the  $l = 1$  resonance, the areas have been equalized. Such a procedure yields an overall error of about 10% for the normalization in correspondence to  $E_{\text{cm}} = 400\text{--}600$  keV and of about 5% in correspondence

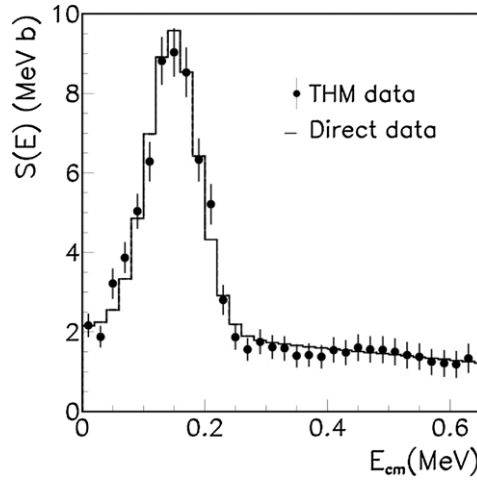


**Figure 13.** THM  $S(E)$ -factor for the  $^{11}\text{B}(p,\alpha_0)^8\text{Be}$  reaction extracted by means of the THM (black points) normalized to the histogram representing the smeared-out function describing the direct bare nucleus extrapolation reported in [28].

to the  $E_{\text{cm}} = 150$  keV resonance, the difference mainly coming from the different statistical uncertainties on the THM data between resonant and non-resonant behaviors.

The astrophysical  $S(E)$ -factor extracted in this work is shown in figure 13, representing the weighted average between the two data sets shown in figure 12. The error bars on the TH experimental points, shown in figure 13, refer only to the statistical one, ranging from  $\sim 10\%$  to  $\sim 20\%$  on the non-resonant part and about  $7\%$  close to the  $\sim 150$  keV resonant level. The errors, shown in figure 13, have been calculated by means of standard error propagation for the weighted average between the two data sets shown in figure 12. The THM bare nucleus astrophysical  $S(E)$ -factor was then fitted using the following analytic function (solid line in figure 14):

$$S(E)_{\alpha_0}^{\text{TH}} = 2.04 - 1.37E + 0.12E^2 + 7.28 \times \exp \left[ -0.5 \left( \frac{E - 0.148}{0.044} \right)^2 \right] \quad (11)$$

leading to the value of  $S(0) = 2.07 \pm 0.41$  MeV b for the zero-energy bare nucleus  $S(E)$ -factor measured via the THM. The total error on  $S(0)$  takes into account the statistical error on the experimental points ( $\sim 10\%$ ) as well as the sources of systematic uncertainties, i.e. the choice of the cut-off radius  $R$  in the calculation of the penetrability through the Coulomb barrier ( $\sim 14\%$ ), the uncertainties on the normalization procedure ( $\sim 10\%$ ). The *measured* value obtained here is in agreement, within the experimental uncertainties, with the *extrapolated* one given in the direct measurement of [28]. It also confirms the preliminary TH investigation made in [32], focused only in a narrow  $\theta_{\text{cm}}$  range. The result obtained here then allowed us to investigate the  $S(E)$  behavior for the angular region  $50^\circ < \theta_{\text{cm}} < 120^\circ$ .

The discrepancy between the present determination and the result reported in the first  $^{11}\text{B}$ -p TH investigation [31] must be ascribed mainly to the presence of sequential mechanisms, i.e. the contribution of the  $^9\text{Be}$  compound nucleus, just in the energy range where the TH data were normalized to the available direct ones [28]. To overcome this difficulty, in this paper, as well as in the preliminary analysis in [32, 33], a strict selection of the kinematical conditions corresponding to a negligible SM contribution was necessary.

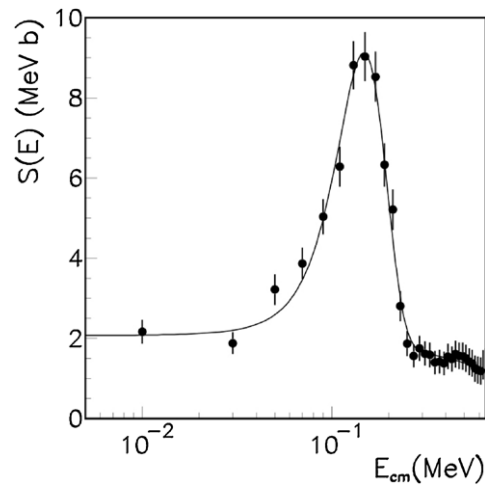


**Figure 14.**  $S(E)$ -factor for the  $^{11}\text{B}(p,\alpha_0)^8\text{Be}$  reaction extracted by means of the THM (black points) with its fit given in terms of equation (11).

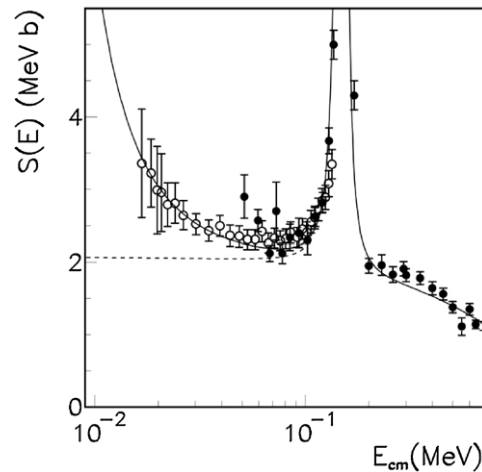


**Figure 15.** Experimental data from [29] (empty circles) ‘re-scaled’ to the experimental data from [28], shown as full circles. The dotted line represents the bare nucleus  $S(E)$ -factor from equation (13) while the full line is the results of our fit taking into account the exponential increase due to the presence of the electron screening potential (see text for details).

### 6.3. Electron screening potential

Once the behavior of the bare nucleus  $S(E)$ -factor was evaluated, the electron screening potential  $U_e$  was determined using the low-energy direct data of [29] normalized to those of [28]. The adopted experimental data are displayed in figure 15; the empty circles are the ‘scaled’ data of [29] and the full circles are the experimental data of [28]. In [29], the authors give the data as a sum of both  $\alpha_0$  and  $\alpha_1$  contributions, with the former  $\sim 1\%$  of the total  $S(E)$ -factor; thus, the 1% of the  $S(E)$ -factor in [29] has been considered. First, the  $U_e$  potential

has been evaluated by fitting the data from [29] with the *extrapolated* bare nucleus  $S$ -factor given in [28], multiplied by the exponential term in equation (1), with  $U_e$  as the only free parameter. This procedure provides a value of  $U_e = 430 \pm 80$  eV, in perfect agreement with that in [29].

Once the procedure has been tested and the data of [29] properly scaled, the same data of [29] have been fitted with the formula

$$S(E)_{\text{sh}} = S(E)_b \times \exp(\pi \eta U_e/E) \quad (12)$$

with  $S(E)_b$  the bare nucleus astrophysical  $S(E)$ -factor given as the sum between the non-resonant contribution, extracted via the THM as in equation (11), and the resonant one reported in [28]:

$$S(E)_b = 2.04 - 1.37E + 0.12E^2 + \frac{0.69 \times 10^{-3}}{(E - 0.148)^2 + 7.13 \times 10^{-6}}. \quad (13)$$

The fit fixes the free parameter  $U_e$  for the  $\alpha_0$  channel to  $U_e^{\text{THM}} = 472 \pm 160$  eV. The dotted line in figure 15 represents the bare nucleus  $S(E)$  factor from equation (13) while the full line is the results of our fit. The  $U_e^{\text{THM}}$  obtained here is in agreement with the value of  $430 \pm 80$  eV reported in [29], though it is higher than the upper limit of 340 eV predicted by the adiabatic limit. The deviation from the adiabatic limit confirms once again the systematic discrepancy between experimental and theoretical values for the electron screening potential (see [7, 8] and references therein), thus leaving the electron screening understanding as an important open question for nuclear physics and astrophysics, as well as atomic physics or condensed matter physics.

## 7. Conclusions

In recent years, several TH investigations have been performed to study the  $^{11}\text{B}(p,\alpha_0)^8\text{Be}$ , yielding discrepant results about the zero-energy  $S(E)$ -factor [31–33]. This called for a new experiment and for an improved data analysis technique to evaluate all the possible sources of systematic uncertainties. In this paper, a new indirect study of the  $^{11}\text{B}(p,\alpha_0)^8\text{Be}$  reaction has been reported. Its  $S(E)$ -factor has been measured applying the THM to the  $^2\text{H}(^{11}\text{B},\alpha_0^8\text{Be})n$  reaction at 27 MeV. The results confirm the presence of a strong QF contribution populating the three-body channel around the region of nearly zero spectator momentum. The THM allowed one to measure the cross section at the Gamow peak, centered here at about  $\sim 10$  keV. Until now, only the extrapolation of [28] provided information on the  $^{11}\text{B}(p,\alpha_0)^8\text{Be}$   $S(E)$ -factor in the astrophysical energy window. This result shows once more the power of the THM to measure in the ultra-low energy region of interest for astrophysics overcoming both the Coulomb barrier and the electron screening effect.

Here the data analysis performed for the recent THM investigation has been carefully discussed. Moreover, to allow an investigation on a wider  $\theta_{\text{cm}}$  angular range, the data of [32, 33] were also considered. For both data sets (shown in figure 12), the experimental resolution was evaluated as about  $\sim 100$  keV thus explaining the experimental width (FWHM) of about 100 keV for the  $E_{\text{cm}} \sim 150$  keV resonance, in the  $^{11}\text{B}(p,\alpha_0)^8\text{Be}$   $S(E)$ -factor, larger than its natural width  $\Gamma \approx 5.5$  keV [58].

A careful evaluation of the background process competing with the QF one was also made. In particular, the same particles  $\alpha_0$ ,  $^8\text{Be}$  and  $n$  in the exit channel can be derived from the QF reaction and from SM as well. A careful selection of the experimental data was then performed to eliminate the background contribution from the decay of  $^5\text{He}_{\text{g.s.}}$  and  $^9\text{Be}$  states, affecting the energy region chosen for the normalization procedure. To this aim, typical experimental spectra

were compared with the simulated ones to evaluate the SM contribution on the experimental data discussed here. In addition, to allow for the investigation of the  $^{11}\text{B}(p,\alpha_0)^8\text{Be}$  in a larger  $\theta_{\text{cm}}$  angular range, the data of [32, 33] were considered. However, with respect to the earlier TH investigation of the  $^{11}\text{B}(p,\alpha_0)^8\text{Be}$  reaction discussed in [31], we discarded the data inside the kinematic region where SM contributions dominate.

An additional source of systematic uncertainties is given by distortions altering the shape of the neutron momentum distribution. For such a reason, the momentum distribution deduced from the Hulthén wavefunction used in the present analysis has been compared with the DWBA distribution evaluated by means of the FRESKO code [61]. From the comparison, we can state that a good agreement between DWBA and PWIA is present, within the experimental uncertainties, for neutron momentum values lower than 40 MeV/ $c$ . The present analysis has pointed out that in the low neutron momentum value range, the uncertainty due to the used form of momentum distribution is negligible, as already shown in other TH works (see for instance [22, 23]).

The extracted value of  $S(0)^{\text{THM}} = 2.07 \pm 0.41$  MeV b is in good agreement with the extrapolated one [28]. To give an evaluation of the electron screening potential for the  $^{11}\text{B}(p,\alpha_0)^8\text{Be}$ , we used data from [29] ‘re-scaled’ to those of [28]. Such a procedure was needed due to the lack of direct data in [28] below 40 keV. The value of  $U_e^{\text{THM}} = 472 \pm 160$  eV is in agreement within the experimental errors with the value of  $U_e = 430 \pm 80$  eV measured in [29] using the total  $\alpha_0$  and  $\alpha_1$  contribution to the  $^{11}\text{B}(p,\alpha)^8\text{Be}$  cross section. However, the value obtained here is higher than the value of  $U_e = 340$  eV predicted by the adiabatic limit, confirming the discrepancy between theoretical predictions and experimental  $U_e$  values. In conclusion, the present indirect study of the  $^{11}\text{B}(p,\alpha_0)^8\text{Be}$  reaction via THM represents the first measurement of the astrophysical  $S(E)$ -factor at the Gamow peak.

The study of the  $^{11}\text{B}(p,\alpha)^8\text{Be}$  is also very interesting for the plasma fusion community, the  $^{11}\text{B}+p$  process being considered as one of the best candidates for the aneutronic fusion ( $T \sim 7 \times 10^9$  K [63]). Moreover, because natural boron contains an  $\sim 20\%$  of  $^{10}\text{B}$  contaminants, further studies are needed to determine the  $^{10}\text{B}(p,\alpha)^7\text{Be}$  cross section. In the case of  $^{11}\text{B}$ , it must be stressed that the main channel for its  $(p,\alpha)$  destruction is the  $^{11}\text{B}(p,\alpha_1)^8\text{Be}$  reaction whose cross section is about two orders of magnitude higher than that of the  $^{11}\text{B}(p,\alpha_0)^8\text{Be}$  one ([30] and references therein). With the same experimental apparatus discussed here, it was possible to detect the alpha particles coming from the de-excitation of the  $^8\text{Be}$  first excited state, meaning the possibility of studying the  $^2\text{H}(^{11}\text{B},\alpha_1^8\text{Be}^*)n$  reaction. However, due to the low statistics and the poor energy resolution for such a channel, a further experiment is needed. For such a reason, and due to the recent observations pointed out in [63] on the  $^{11}\text{B}(p,\alpha_1)^8\text{Be}$  reaction mechanism, much effort must be made to measure the  $\alpha_1$  contribution of such a reaction via the THM.

## Acknowledgments

The authors wish to thank Bakhadir Irgaziev for his fruitful contribution during the preparation of the manuscript. This work was supported in part by the Italian Ministry of the University under grant RBFR082838. VB, VK, ZH and JM acknowledge the support of LC 07050 of the Czech MŠMT, the grant of the Czech Academy, no M10480902 and the grant of GAČR, no P203/10/310. AM acknowledges the US Department of Energy under grant nos DE-FG02-93ER40773 and DE-FG52-06NA26207, NSF under grant no PHY-0852653.

## References

- [1] Boesgaard A M 2004 The light elements: lithium, beryllium, and boron *Origin and Evolution of the Elements (Carnegie Observatories Astrophysics Series vol 4)* ed A McWilliam and M Rauch (Cambridge: Cambridge University Press)
- [2] Stephens A *et al* 1997 *Astrophys. J.* **491** 339
- [3] Boesgaard A M *et al* 2004 *Astrophys. J.* **605** 864
- [4] Boesgaard A M 2004 arXiv:astro-ph/0412198v1
- [5] Boesgaard A M *et al* 2005 *Astrophys. J.* **621** 991
- [6] Rolfs C and Rodney W 1988 *Cauldrons in the Cosmos* (Chicago, IL: University of Chicago Press)
- [7] Assenbaum H J *et al* 1987 *Z. Phys. A* **327** 461
- [8] Strieder F 2001 *Naturwissenschaften* **88** 461
- [9] Spitaleri C *et al* 1999 *Phys. Rev. C* **60** 055802
- [10] Spitaleri C *et al* 2001 *Phys. Rev. C* **63** 055801
- [11] Lattuada M *et al* 2001 *Astrophys. J.* **562** 1076–80
- [12] Pizzone R G *et al* 2003 *Astron. Astrophys.* **398** 423–7
- [13] Tumino A *et al* 2003 *Phys. Rev. C* **67** 065803
- [14] La Cognata M *et al* 2005 *Phys. Rev. C* **72** 065802
- [15] Tumino A *et al* 2005 *Eur. Phys. J. A* **25** 649
- [16] Tumino A *et al* 2006 *Eur. Phys. J. A* **27** 243
- [17] Lamia L *et al* 2007 *Nucl. Phys. A* **787** 309c
- [18] Tumino A *et al* 2007 *Phys. Rev. Lett.* **98** 252502
- [19] La Cognata M *et al* 2007 *Phys. Rev. C* **76** 065804
- [20] La Cognata M *et al* 2008 *Phys. Rev. Lett.* **101** 152501
- [21] Tumino A *et al* 2008 *Phys. Rev. C* **78** 064001
- [22] La Cognata M *et al* 2010 *Astrophys. J.* **708** 796
- [23] Sergi M L *et al* 2010 *Phys. Rev. C* **82** 032801
- [24] Gulino M *et al* 2010 *J. Phys. G: Nucl. Part. Phys.* **37** 125105
- [25] Pizzone R G *et al* 2011 *Phys. Rev. C* **83** 045801
- [26] Segel R E *et al* 1965 *Phys. Rev.* **139** B818
- [27] Davidson J M *et al* 1979 *Nucl. Phys. A* **315** 253
- [28] Becker H W *et al* 1987 *Z. Phys. A* **327** 341
- [29] Angulo C *et al* 1993 *Z. Phys. A* **345** 231
- [30] Angulo C *et al* 1999 *Nucl. Phys. A* **656** 3
- [31] Spitaleri C *et al* 2004 *Phys. Rev. C* **69** 055806
- [32] Lamia L *et al* 2008 *Nuovo Cimento* **31** 423
- [33] Spitaleri C *et al* 2009 *AIP Conf. Proc.* **1120** 171
- [34] Baur G *et al* 1986 *Phys. Lett. B* **178** 135
- [35] Spitaleri C *et al* 1990 *Problem of Fundamental Modern Physics: II* ed R Cherubini, P Dalpiaz and B Minetti (Singapore: World Scientific) pp 21–36
- [36] Lattuada M *et al* 1985 *Nucl. Phys. A* **458** 493
- [37] Calvi G *et al* 1990 *Phys. Rev. C* **41** 1848
- [38] Zadro M *et al* 1989 *Phys. Rev. C* **40** 181
- [39] Typel S *et al* 2000 *Few Body Syst.* **29** 7
- [40] Typel S *et al* 2003 *Ann. Phys.* **305** 228
- [41] Mukhamedzhanov A *et al* 2008 *J. Phys. G: Nucl. Part. Phys.* **35** 014016
- [42] Cherubini S *et al* 1996 *Astrophys. J.* **457** 855
- [43] Shapiro I S 1962 *Nucl. Phys.* **38** 327
- [44] Shapiro I S 1967 *Proc. XXXVIII Int. School of Physics 'Enrico Fermi'* (New York: Academic) p 210
- [45] Shapiro I S 1968 *Sov. Phys.—Usp.* **10** 515
- [46] Chew G F and Wick G C 1952 *Phys. Rev.* **85** 636
- [47] Neudatchin U *et al* 1965 *At. Energy Rev.* **3** 157
- [48] Jacob G and Maris Th A J 1966 *Rev. Mod. Phys.* **38** 121
- [49] Fallica P G *et al* 1978 *Lett. Nuovo Cimento* **22** 13
- [50] Spitaleri C *et al* 2011 *Phys. At. Nucl.* at press
- [51] Grossiodor J Y *et al* 1974 *Phys. Rev. Lett.* **32** 177

- [52] Chant N S and Roos P G 1977 *Phys. Rev. C* **15** 57
- [53] Roos P G *et al* 1981 *Phys. Rev. C* **24** 2647
- [54] Mukhamedzhanov A 2011 *Phys. Rev. C* submitted
- [55] Barbarino S *et al* 1980 *Phys. Rev. C* **21** 1104
- [56] Pizzone R G 2005 *Phys. Rev. C* **71** 058801
- [57] Pizzone R G *et al* 2009 *Phys. Rev. C* **80** 025807
- [58] Ajzenberg-Selove F 1988 *Nucl. Phys. A* **490** 1
- [59] Audi G and Wapstra A H 1995 *Nucl. Phys. A* **595** 409–80
- [60] Jain M 1970 *Nucl. Phys. A* **153** 49
- [61] Thompson I J *et al* 1987 *Comput. Phys. Rep.* **7** 167
- [62] Perey C M and Perey F G 1976 *At. Data Nucl. Data Tables* **17** 1
- [63] Stave S *et al* 2011 *Phys. Lett. B* **696** 26–9